Limits of the cylindrical absorber design for a sodium receiver

Cite as: AIP Conference Proceedings **2033**, 040006 (2018); https://doi.org/10.1063/1.5067042
Published Online: 08 November 2018

Charles-Alexis Asselineau, William Logie, John Pye, and Joe Coventry

Limits of the Cylindrical Absorber Design for a Sodium Receiver

Charles-Alexis Asselineau[1,a)], William Logie[1], John Pye[1] and Joe Coventry[1]

[1]*Research School of Engineering, Australian National University, Canberra, ACT 0200 Australia.*

[a)] Corresponding author: charles-alexis.asselineau@anu.edu.au.

Abstract. The applicability of the cylindrical arrangement of vertical tube banks is evaluated for liquid sodium concentrating solar thermal receivers and compared with a molten salt reference case through a series of parametric studies. It is shown that sodium receivers experience less thermo-elastic stress load and can operate under higher flux which presents advantages in terms of size reduction and efficiency. While the cylindrical receiver configuration cannot reach the efficiency target of 91% in a high temperature configuration (480 °C to 640 °C), there is potential to improve efficiency by improving heliostat field optics. Flux limitations due to thermo-elastic stresses are less stringent due for sodium receivers due to the better heat transfer properties, and consequently better heliostat field optics would benefit sodium receiver concepts more than molten salts ones.

INTRODUCTION

Liquid sodium is investigated as a heat carrier for the next generation of concentrating solar thermal power (CSP) systems. Liquid sodium has interesting heat transfer characteristics: good thermal conductivity, low viscosity and a large liquidus from 100 °C to 870 °C in typical operation conditions. Liquid sodium could bring a range of economical benefits to CSP systems if it was to replace molten salts in the receiver. The higher temperature of operation could enable the use of higher efficiency power cycles, such as sCO2 Brayton or combined Brayton/Rankine cycles that have a higher exergetic efficiency and therefore have the potential to generate more revenue. The higher incident flux on the absorber could lead to higher receiver thermal efficiencies[1] and smaller receiver volume, contributing to an increase in revenue and decrease in capital cost. Additionally, the good heat transfer properties of sodium could lead to lower thermo-mechanical stress on the absorber components at identical flux when compared with other heat carriers[2]. Numerous potential barriers for the successful deployment of sodium receivers, not treated in this study include: absorber material corrosion through a range of mechanisms[3]; liquid sodium unsuitability as a thermal energy storage medium, from the combined effect of a low density and low heat capacity; and the added hazard mitigation cost on the liquid sodium loop because of the risk of reaction between sodium and water[4]. Liquid sodium was considered as the heat carrier of choice for the Liquid Metal Fast Breeder Reactor (LMFBR) system and significant work has been conducted to tackle these issues. Liquid sodium has been shown to enable CSP system operation under high incident radiative flux when used as a heat transfer fluid (HTF) for solar receivers[5]. Values of 1.8 $MW.m^{-2}$ of peak incident flux have been suggested in the literature for sodium receivers as acceptable design limits for 30 years lifetime[6], which compares to 1.2 $MW.m^{-2}$ molten salt receivers[7]. Billboard, cavity and cylindrical type receivers have been suggested as candidate geometries for liquid sodium receivers[4, 8]. The cylindrical geometry is currently the state-of-the-art for molten salt central receiver systems. In this study we are evaluating the applicability of the surrounding heliostat field and cylindrical receiver concept to liquid sodium receivers. This work is developed as part of the Australian Solar Thermal Research Initiative (ASTRI) effort to design a 91% efficient receiver for a new high temperature CSP system[9]. The current configuration of interest targets a 25 MWe liquid sodium receiver operating between 480 °C and 640 °C[10]. The aim of this work is to explore the limits of efficiency for cylindrical sodium receiver designs operating at such temperatures, and provide guidance for future receiver designs.

SolarPACES 2017
AIP Conf. Proc. 2033, 040006-1–040006-9; https://doi.org/10.1063/1.5067042
Published by AIP Publishing. 978-0-7354-1757-1/$30.00

MODELS AND SIMULATION

System Model

The optical concentrator considered in this study is the ASTRI reference field composed of 6177 heliostats each with an area of 31.27 m^2 and located near Alice Springs, Australia, presented in Figure 1[10]. The heliostats are composed of 4 square facets covering 97% of the heliostat aperture, have an ideal individual focal length and are moved according to an aiming strategy described in the "Simulation Tools" section. The reflectivity of the heliostat facets is assumed to be 90% and the overall reflected beam error characterised with a single surface slope error value in both x and y projected directions on the heliostat plane. This surface slope error value is a variable in the upcoming parametric analysis.

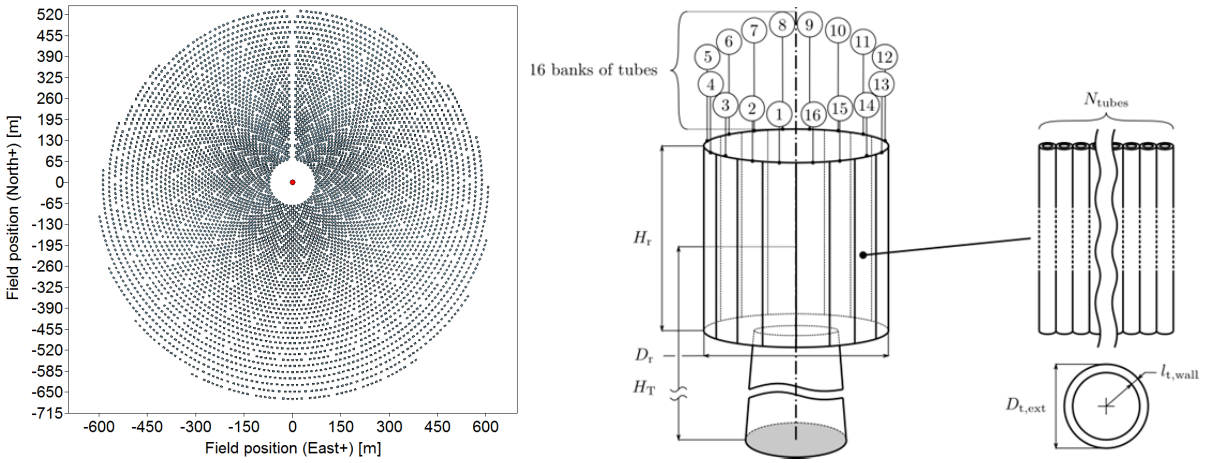

FIGURE 1. The ASTRI reference heliostat field and receiver schematic diagram.

The receiver is composed of 16 vertical banks of parallel tubes as shown in Figure 1. The height of the receiver mid-point is fixed to 91.1 m, the value that was used for the design of the heliostat field layout. The height and diameter of the receiver, the tube dimensions and the number of tubes per bank are variables that will be studied in the parametric study presented in the rest of this study. Two standard nominal pipe sizes (Table 1) are considered in this study. DN 32 is the closest pipe dimension to the reported values in Rodríguez-Sánchez et al.[11] and is therefore used in the molten salt receiver reference case. DN 10 is also considered as an alternative case because of the thinner wall thickness and potential associated benefits on receiver efficiency, despite the smaller tube diameter.

TABLE 1. Standard pipe sizes considered.

NPS	DN	$D_{t,ext}$	$l_{t,wall}$
⅜	10	17.15 mm	1.245 mm
1¼	32	42.16 mm	1.651 mm

The receiver flow-path is presented in Figure 2 for configurations with two and eight parallel channels. The HTF is introduced at the top of the receiver on the south facing banks and progresses along the profile until reaching the west-east axis. At that point the flow-paths cross the receiver cylinder and continue to flow along the banks on the north facing side of the receiver following an axial symmetry. The receiver tubes are assumed to be made of Haynes 230® alloy and the thermo-mechanical and thermal conductivity values are obtained from manufacturer datasheet[12]. For the molten salt reference configuration, Solar Salt (60 wt% $NaNO_3$, 40 wt% KNO_3) is considered and the heat transfer and the incompressible thermo-physical properties are sourced from Benoit et al.[13]. The liquid sodium incompressible properties are sourced from Fink and Leibowitz[14]. The external walls of the tubes are assumed to be

coated with Pyromark 2500® paint and an absorptivity of 0.94 is assumed for the visible fraction of the electromagnetic spectrum and 0.89 for the rest of the spectrum[15].

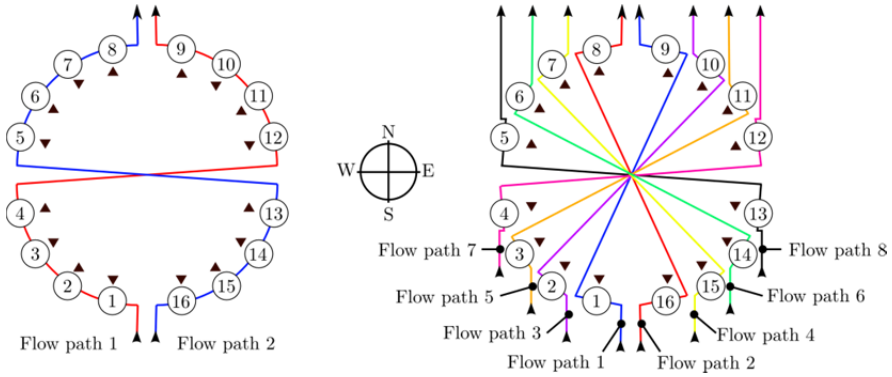

FIGURE 2. Illustration of the receiver flow-pathing for 2 and 8 parallel flow-paths.

Energy Balance

The energy balance is established by coupling the radiative flux incident on the external wall of the receiver tubes for the equinox noon with a heat transfer model describing the increase in temperature of the HTF as it progresses through each flow path. The receiver aperture is discretised into 16 banks and 50 vertical elements per bank resulting in 800 surface elements, each accounting for N_{tubes} parallel tubes in a specific bank over a small flow-path length. Each flow-path supports an independent 1-D model that is mapped onto the receiver surface incident fluxmap. Thermal emissions and the external convective loss are calculated using the local external temperature of the tubes. The conduction through half the tube wall is used to determine the local inner wall temperature of the tubes. The enthalpy gain of the HTF is determined using relevant heat transfer correlations[13]. Three efficiency metrics are used in this study. The intercept factor η_{int} quantifies the fraction of the radiation reflected by the heliostat field that is actually intercepted by the receiver. The thermal efficiency η_{th} evaluates the efficiency of the conversion of the intercepted radiation into heat carried out of the receiver by the HTF. The product of these two efficiencies gives a measure of the receiver efficiency $\eta_{\text{rec}} = \eta_{\text{int}}\eta_{\text{th}}$.

Thermo-Elastic Stress Model

Thermoelastic stress is calculated using a conventional steady-state method which assumes that the non-axisymmetrically heated tubes are steady-state and a harmonic Fourier solution exists. First, the radial and circumferential temperature distribution are solved using the Gauss-Seidel iterative scheme before coefficients for the harmonic solution are sought using a least-squares fit to the inner and outer tube surface temperatures. The classical method was implemented in a Python script and validated using a solid mechanics solver from the OpenFOAM(R) toolbox[16].

Simulation Tools

Simulation of the concentration of solar radiation incident on the heliostat field to the receiver aperture is handled using a cone optics code, SolarPILOT from NREL[17]. SolarPILOT uses a fast Hermite polynomial expansion method to compute flux distributions on simple receiver shapes, such as the cylindrical receiver arrangement. In this study, solar radiation is modelled using a uniform angular distribution of intensity over the solar disk (0 to 4.65 mrad), also known as the "pillbox" sunshape. The solar radiation is reflected by the heliostat facets in the field towards the receiver. The aiming of the heliostats on the receiver is determined using an aiming strategy called "Image Size Priority" (ISP) in SolarPILOT to distribute the flux on the receiver aperture. With cylindrical receiver targets, ISP builds an aiming grid with the centre of each receiver aperture surface element and always assigns heliostat aim-points to the closest tube bank. The heliostat aiming point is therefore constrained to a vertical position

variation along the closest tube bank. An aiming parameter, which is a multiple of the standard deviation of the heliostat vertical flux distribution on the receiver, determines an acceptable vertical aiming region for each heliostat. Heliostat aiming points are determined in a decreasing projected image size order, as the position where the flux is lowest in their respective acceptable aiming region. The solution of the receiver energy balance is conducted in a Python-based model using a 1-D staggered grid mesh for each flow-path as described earlier. The solution of the system is realised through nested iterative bisection loops with an absolute convergence criterion on temperature values of 0.001 K.

Parametric Studies

A parametric study is developed to evaluate the conjoint influence of the receiver geometry, the surface slope error of the mirrors and the aiming strategy parameter on the receiver efficiencies.

TABLE 2. Parameter space summary.

	Minimum	Maximum	Increment
Receiver height	6 m	10 m	0.5 m
Receiver diameter	6 m	10 m	0.5 m
Heliostat surface slope error	0.9 mrad	1.5 mrad	0.3 mrad
SolarPILOT ISP parameter	0	2.5	0.5

1458 optical simulations are realised to cover the full parameter space. The fluxmaps and field efficiency summary data are stored in a database and re-used for each of the four receiver efficiency studies presented in the next section. These studies include a reference case solar salt receiver followed by sodium receiver studies within the same temperature and flux constraints[7] of 1.2 $MW.m^{-2}$ and the two pipe sizes considered. The flux constraint is then relaxed[6] to 1.8 $MW.m^{-2}$ on the sodium receiver designs, and then the temperature of operations increased to the level identified in the ASTRI configuration mentioned in the introduction. Table 3 summarises the receiver studies in this paper. In total, 10206 energy balance simulations are conducted to simulate all the receiver configurations.

TABLE 3. Receiver energy balance parametric studies.

HTF	Tube size	Peak flux	Inlet temperature	Outlet temperature
Solar salt	DN 32	1.2 $MW.m^{-2}$	290 °C (563.15 K)	565 °C (838.15 K)
Liquid sodium	DN 10	1.2 $MW.m^{-2}$	290 °C (563.15 K)	565 °C (838.15 K)
Liquid sodium	DN 32	1.2 $MW.m^{-2}$	290 °C (563.15 K)	565 °C (838.15 K)
Liquid sodium	DN 10	1.8 $MW.m^{-2}$	290 °C (563.15 K)	565 °C (838.15 K)
Liquid sodium	DN 32	1.8 $MW.m^{-2}$	290 °C (563.15 K)	565 °C (838.15 K)
Liquid sodium	DN 10	1.8 $MW.m^{-2}$	480 °C (753.15 K)	640 °C (913.15 K)
Liquid sodium	DN 32	1.8 $MW.m^{-2}$	290 °C (563.15 K)	565 °C (838.15 K)

RESULTS

Optical Simulations

Figure 3 (a) presents the intercept factor for each of the 1458 configurations as a function of the peak incident flux on the receivers and highlights the dominating influence of the aiming strategy on the spillage fraction. The higher the aiming parameter the "tighter" the aiming region on the receivers and therefore the less spillage is allowed; conversely, the lower the aiming parameter, the "looser" the aiming region and the more spillage occurs. Intercept factors over 95% can only be reached with aiming parameters of 1.5 or more. For a given aiming parameter, heliostats with smaller surface slope error always perform better as higher intercept factors can be obtained for a given peak flux and aiming parameter.

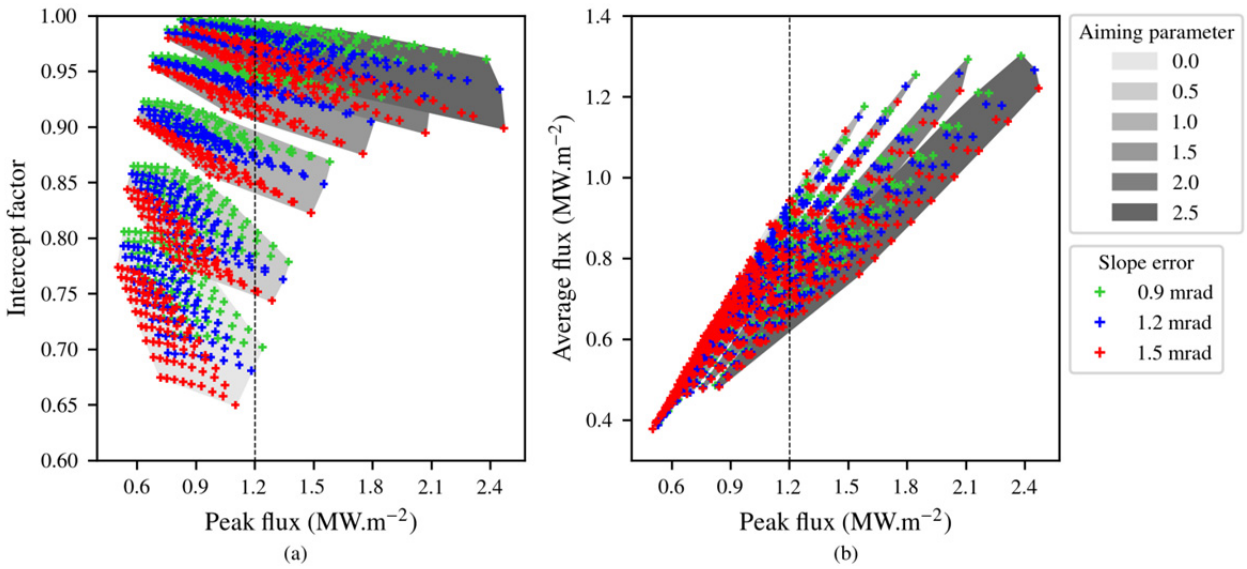

FIGURE 3. (a) Intercept factor and (b) average intercepted flux plotted against the peak intercepted flux for all simulated configurations. The vertical dashed lines represent two characteristic peak flux limits: 1.2 MW.m^{-2} and 1.8 MW.m^{-2}.

In Figure 3 (b), the peak and average incident fluxes on the receivers are compared. A higher peak flux is generally associated with a higher average flux. The aiming strategy impacts the average flux that can be reached at a given peak flux limit, with loose aiming providing higher average fluxes at a given peak flux limit, but able to reach lower flux values overall. The broadening of the aiming parameter regions highlights the stronger influence of the mirror quality on the achievable average flux for tighter aiming strategies.

Receiver Energy Balance Simulations

The thermal efficiency of the 1458 configurations running with solar salt as the HTF and DN 32 tubes is presented in Figure 4 (a). The thermal efficiency is higher with higher receiver peak flux. As shown earlier, a higher peak flux is correlated to a higher average flux on the receiver, which has a positive impact on the conversion of radiation into heat. In addition, looser aiming give higher average flux at a given peak flux value and therefore have a higher thermal efficiency. The thermal efficiency follows an opposite trend to the intercept efficiency variation with regard to peak flux and a trade-off appears when multiplying them to obtain the receiver efficiency plotted in Figure 4 (b). Smaller receivers have higher spillage but they also have higher thermal efficiency because the average flux is higher. Overall, tighter aiming strategies improve the receiver efficiency and the intercept factor gains obtained from using better mirrors remain in the receiver efficiency.

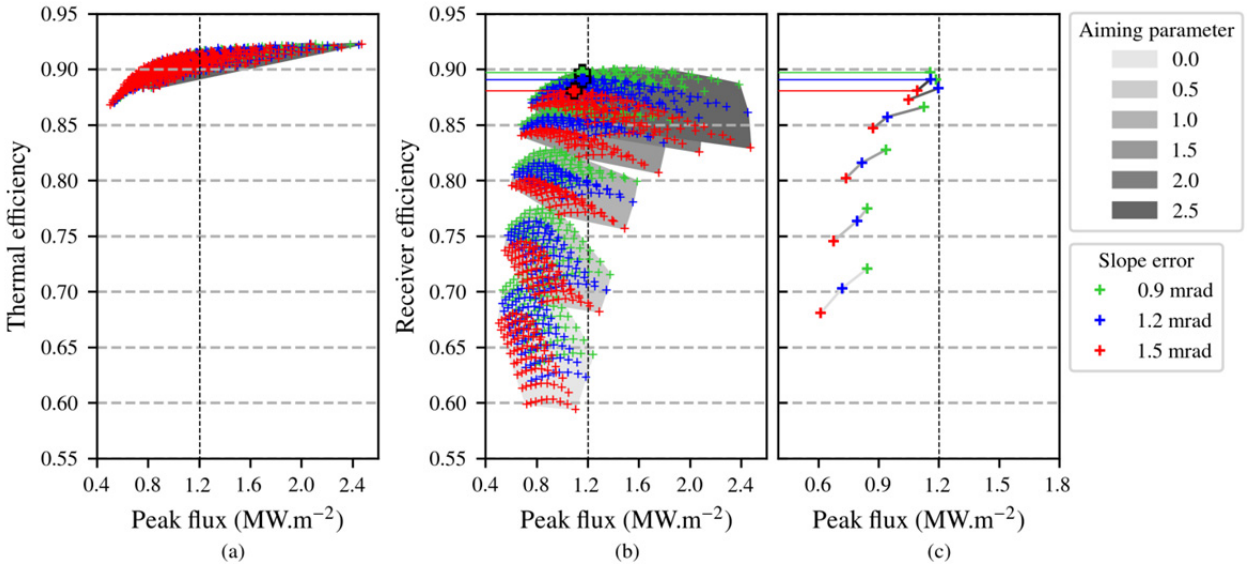

FIGURE 4. (a) Thermal efficiency and (b) receiver efficiency of all candidates, as a function of the peak flux for reference conditions solar salt receivers. The best performing candidates in each combination of aiming strategy and heliostat surface slope error are shown in (c). The vertical line marks the 1.2 MW.m^{-2} flux limitation considered and the three highlighted configurations are the best performing ones for each heliostat surface slope error.

Table 4 presents the best configurations that respect the 1.2 MW.m^{-2} peak flux limit for each of the mirror surface slope error considered. The receiver radii are the same for the three configurations, however, the height of the receiver is slightly higher for the less accurate mirrors (1.5 mrad of slope error). The peak flux of the 0.9 mrad and 1.2 mrad configurations are very close to the peak flux limit: the receiver efficiency is constrained by the imposed flux limitation, however, for the 1.5 mrad case, the best receiver efficiency occurs for a configuration with a lower peak flux. These observations are confirmed when looking at Figure 4 (b) for the highest aiming parameter values where the maximum receiver efficiency is on the right of the black line for the green and blue crosses but on the left for the red crosses. Overall the better heliostats provide an improvement of 1.7% in receiver efficiency, mostly due to better intercept factor. The calculated thermo-elastic stress values are high and mostly driven by high compressive axial stress on the external region of the tube that receives the highest flux as reported by Logie et al.[2] and significantly over the typical ASME boiler and pressure vessel code rules usually considered in the design of receivers[11].

TABLE 4. Best solar salt receiver reference (cf. TABLE 3) configurations for the three heliostat surface slope errors considered.

Slope error (mrad)	0.9	1.2	1.5
Radius (m)	4.0	4.0	4.0
Height (m)	9.0	9.0	9.5
Aperture area (m^2)	226.2	226.2	238.8
Peak flux ($MW.m^{-2}$)	1.156	1.158	1.091
Intercept efficiency	0.994	0.988	0.979
Thermal efficiency	0.903	0.902	0.900
Receiver efficiency	0.898	0.891	0.881
Maximum Von-Mises stress (MPa)	467.4	473.2	457.1

The heat transfer fluid is now changed to liquid sodium and the energy balance for each of the 1458 configurations is simulated again, first for the same inlet and outlet temperatures, then for an inlet of 480 °C and an outlet of 640 °C, with both pipe sizes. The number of parallel flow-paths is adapted for each receiver configuration to ensure that the sodium velocity in the pipes never exceeds 6 $m.s^{-1}$ based recommendations in the Sodium-NaK Engineering Handbook[3]. The best geometries for each combination of mirror slope error, aiming parameter and pipe sizes are presented in Figure 5.

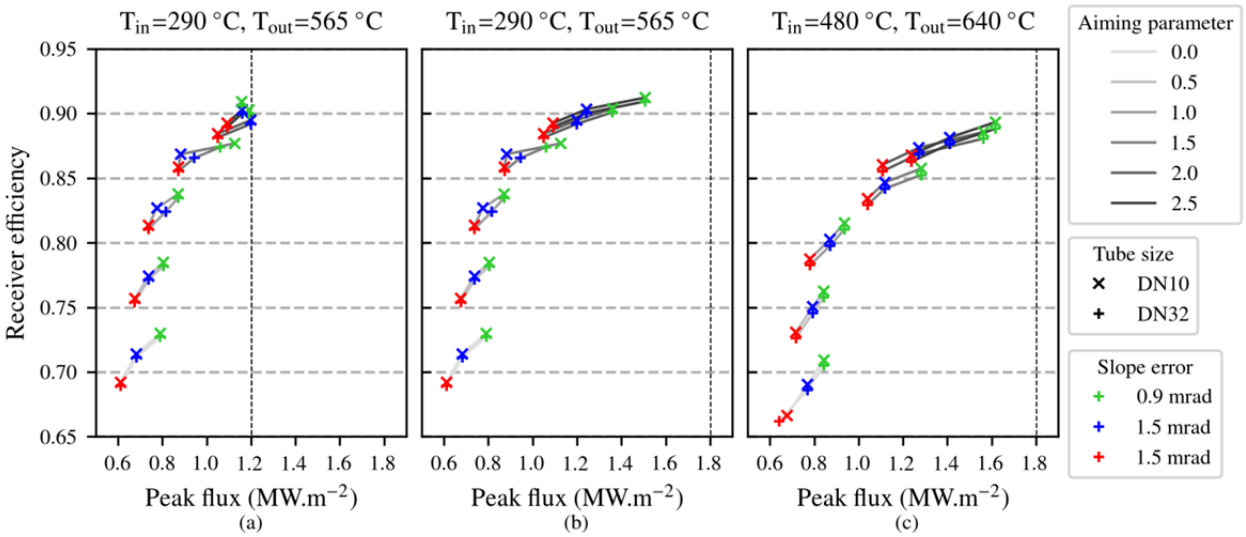

FIGURE 5. Receiver efficiency for the best sodium receiver configurations as a function of the receiver aperture peak flux for (a) HTF temperatures between 290 °C and 565 °C and a flux limit of 1.2 $MW.m^{-2}$, (b) HTF temperatures between 290 °C and 565 °C and a flux limit of 1.8 $MW.m^{-2}$ and (c) HTF temperatures between 480 °C and 640 °C and a flux limit of 1.8 $MW.m^{-2}$.

Configurations in Figure 5 (a) and (b) belong to the same set of energy balance results but were selected according to different flux limits, hence resulting in identical best receiver configurations where the peak flux is not a limitation. The best geometries for the aiming parameters of 2 and 2.5 are slightly different because higher quality mirrors push the best receiver efficiency beyond 1.2 $MW.m^{-2}$. At higher temperatures (Fig 5 (c)), receiver efficiencies drop and are reached at slightly higher peak fluxes: as heat loss increases, smaller receivers perform better and sacrificing a bit more spillage is favourable. At no point is the sodium receiver performance limited by the 1.8 $MW.m^{-2}$ limit. Overall the performance of thinner, smaller diameter pipes is always marginally higher, with slightly better improvement at higher temperatures. Table 5 summarises the performance of the best receiver efficiency geometries for each sodium receiver study.

TABLE 5. Performance summary of the best configurations for the three sodium receiver scenarios considered.

HTF temperature (°C)	290 -> 565						290 -> 565						480 -> 640					
Flux limit ($MW.m^{-2}$)	1.2						1.8						1.8					
Tube DN	10			32			10			32			10			32		
Slope error (mrad)	0.9	1.2	1.5	0.9	1.2	1.5	0.9	1.2	1.5	0.9	1.2	1.5	0.9	1.2	1.5	0.9	1.2	1.5
Radius (m)	4	4	4	4	4	4	3.75	4	4	3.75	4	4	3.5	3.75	4	3.5	3.75	4
Height (m)	9	9	9.5	9	9	9.5	7.5	8.5	9.5	7.5	8.5	9.5	7.5	8	8.5	7.5	8	8.5
Aperture area (m^2)	226	226	239	226	226	239	177	214	239	177	214	239	165	189	214	165	189	214
Peak flux ($MW.m^{-2}$)	1.16	1.16	1.09	1.16	1.16	1.09	1.51	1.24	1.09	1.51	1.24	1.09	1.62	1.41	1.24	1.62	1.41	1.24
Intercept efficiency	0.99	0.99	0.98	0.99	0.99	0.98	0.99	0.99	0.98	0.99	0.99	0.98	0.99	0.98	0.97	0.99	0.98	0.97
Thermal efficiency	0.92	0.91	0.91	0.91	0.91	0.91	0.92	0.92	0.91	0.92	0.91	0.91	0.91	0.90	0.89	0.90	0.90	0.89
Receiver efficiency	0.91	0.90	0.89	0.91	0.90	0.89	0.91	0.90	0.89	0.91	0.90	0.89	0.89	0.88	0.87	0.89	0.88	0.86
Max. Von-Mises stress (MPa)	241	236	221	295	300	284	308	253	221	388	320	284	284	248	215	370	330	294

Comparing with the molten salt results (Table 4), liquid sodium shows improved thermal efficiencies leading to slightly higher receiver efficiencies in the 290 °C to 565 °C temperature range. When considering higher flux limit (1.8 $MW.m^{-2}$), the dimensions of the receiver aperture are greatly reduced with mirror slope errors of 0.9 mrad and 1.2 mrad. Peak thermo-elastic stress values are generally much lower than with solar salt. In the 290°C to 565°C temperature range, thermal stress is increased by the increase in flux but the rise to the 480°C to 640°C range does not further increase stress. In fact the peak stress at higher temperatures is reduced with mirror slope errors of 0.9 mrad and 1.2 mrad due to favourable material properties. Finally, the DN 10 pipes experience significantly less thermo-elastic stress than the DN 32 ones.

DISCUSSION

From this study, it appears that a cylindrical sodium receiver concept is not able to reach the ASTRI target of 91% receiver efficiency for the in the 480°C to 640°C temperature range and can only reach 91% thermal efficiency of with DN10 tubes and high quality 0.9 mrad error mirrors. Higher temperatures would give access to higher efficiency when converting heat into work but this is outside the scope of this study. Physical limitations exist for a cylindrical solar salt receiver (thermo-elastic stress, salt decomposition) and impose a flux limitation that negates the potential positive impact of improvements in the optical quality of the field. Sodium concepts do not suffer from the same problem and show much lower stress which enables cylindrical sodium receivers to more fully benefit of optical efficiency improvements. Consequently, improving the optical efficiency of the concentrator would benefit sodium receiver concepts more than molten salts ones.

Cylindrical sodium receivers are found to be potentially much smaller than their molten-salts counterpart. The use of thin and small diameter pipes is found to greatly reduce thermo-elastic stress and marginally improve thermal efficiency, but impose changes on the receiver flow-path. Changing the receiver design to a cavity-like geometry could provide both gains in optical efficiency, as the flux on the aperture can then be much higher, and reductions in energy losses are expected[18, 19].

AKNOWLEDGEMENT

The authors would like to aknowledge ASTRI for its support. The ASTRI program has been supported by the Australian Government through the Australian Renewable Energy Agency (ARENA). The Australian Government, through ARENA, is supporting Australian research and development in solar photovoltaic and solar thermal technologies to help solar power become cost competitive with other energy sources. The views expressed herein

are not necessarily the views of the Australian Government, and the Australian Government does not accept responsibility for any information or advice contained herein.

REFERENCES

1. K. Lovegrove and J. Pye, in *Concentrating Solar Power Technology*, edited by K. Lovegrove and W. Stein (Woodhead Publishing, 2012), pp. 16-67.
2. W. Logie, J. D. Pye and J. Coventry, presented at the Proceedings of the APSRC 2016, 2016 (unpublished).
3. O. J. Foust, *Sodium-NaK engineering handbook*. (New York : Gordon and Breach, 1972).
4. J. Coventry, C. Andraka, J. Pye, M. Blanco and J. Fisher, Solar Energy **122**, 749-762 (2015).
5. W. J. C. Schiel, M. Geyer and R. Carmona, *The IEA/SSPS High Flux Experiment*. (Springer-Verlag, 1987).
6. B. D. Pomeroy, J. M. Roberts and T. V. Narayanan, Journal of Solar Energy Engineering **103** (1), 52-55 (1981).
7. M. R. Rodríguez-Sánchez, A. Soria-Verdugo, J. Z. A. Almendros-Ibáñez, A. Acosta-Iborra and D. Santana, Applied Thermal Engineering **63** (1), 428-438 (2014).
8. N. Boerema, G. Morrison, R. Taylor and G. Rosengarten, Solar Energy **97**, 356-368 (2013).
9. J. Coventry, M. Arjomandi, C.-A. Asselineau, A. Chinnici, C. Corsi, D. Davis, J.-S. Kim, A. Kumar, W. Lipinski, W. Logie, G. Nathan, J. Pye and W. Saw, AIP Conference Proceedings **1850** (1), 030011-030011 (2017).
10. ASTRI, (http://www.astri.org.au, 2017).
11. A. Sánchez-González, M. R. Rodríguez-Sánchez and D. Santana, Solar Energy, - (2016).
12. Haynes, (http://haynesintl.com/, 2018).
13. H. Benoit, L. Spreafico, D. Gauthier and G. Flamant, Renewable and Sustainable Energy Reviews **55**, 298-315 (2016).
14. J. K. Fink and L. Leibowitz, 1995.
15. C. K. Ho, A. R. Mahoney, A. Ambrosini, M. Bencomo, A. Hall and T. N. Lambert, Journal of Solar Energy Engineering **136** (1), 014502-014502 (2013).
16. W. R. Logie, J. D. Pye and J. Coventry, Solar Energy **160**, 368-379 (2018).
17. NREL, (https://www.nrel.gov/csp/solarpilot.html, 2016).
18. C.-A. Asselineau, The Australian National University, 2018.
19. C.-A. Asselineau, C. Corsi, J. Coventry and J. Pye, AIP Conference Proceedings **1850** (1), 030002 (2017).